

Lifespan of mountain ranges scaled by feedbacks between landsliding and erosion by rivers

David L. Egholm¹, Mads F. Knudsen¹ & Mike Sandiford²

An important challenge in geomorphology is the reconciliation of the high fluvial incision rates observed in tectonically active mountain ranges with the long-term preservation of significant mountain-range relief in ancient, tectonically inactive orogenic belts^{1–3}. River bedrock erosion and sediment transport are widely recognized to be the principal controls on the lifespan of mountain ranges. But the factors controlling the rate of erosion^{4–8} and the reasons why they seem to vary significantly as a function of tectonic activity remain controversial. Here we use computational simulations to show that the key to understanding variations in the rate of erosion between tectonically active and inactive mountain ranges may relate to a bi-directional coupling between bedrock river incision and landslides. Whereas fluvial incision steepens surrounding hillslopes and increases landslide frequency⁹, landsliding affects fluvial erosion rates in two fundamentally distinct ways. On the one hand, large landslides overwhelm the river transport capacity and cause upstream build up of sediment that protects the river bed from further erosion^{9–11}. On the other hand, in delivering abrasive agents to the streams^{4–6}, landslides help accelerate fluvial erosion. Our models illustrate how this coupling has fundamentally different implications for rates of fluvial incision in active and inactive mountain ranges. The coupling therefore provides a plausible physical explanation for the preservation of significant mountain-range relief in old orogenic belts, up to several hundred million years after tectonic activity has effectively ceased.

The erosive power of rivers incises bedrock in mountain belts and forms self-organizing patterns characteristic of dendritic drainage systems. Bedrock incision occurs by a combination of processes related to the transport of both water and sediment within the rivers^{4–8}. The balance between these erosion processes is poorly understood, and models for fluvial landscape evolution often rely on the assumption that river erosion rates scale with some measure of flow intensity, such as stream power¹² or shear stress¹³, which are both simple functions of local relief and water discharge. These models, collectively referred to as ‘stream-power models’, have found widespread favour in the modelling community, because they reproduce many features observed in natural landscapes^{12–15}.

However, stream-power models do not adequately capture the role of mobile sediment in fluvial erosion, and a number of recent studies of long-term erosion rates based on field measurements, low-temperature thermochronology and cosmogenic nuclides show that variations in precipitation rate^{16–19} and topographical relief^{20,21}, and, hence, stream power, do not always account for the long-term erosion rate of bedrock landscapes. Instead, measurements of average catchment denudation rates suggest that erosion is fast primarily where active tectonism constantly rejuvenates the topographic surface^{1,2,16,19–21} but slow in many high-relief passive orogens^{1,2,22,23}, which require nonlinear couplings between relief, discharge and erosion that are not easily explained by the stream-power concept. In particular, the long-term preservation of kilometre-scale mountainous relief in ancient, tectonically inactive, Palaeozoic orogenic belts, such as the Appalachian mountains in the United States, the Ural mountains in Russia and the Caledonian mountains in Greenland and Scandinavia (Supplementary Fig. 1), seems

directly at odds with the stream-power concept for river erosion. Although post-orogenic uplift processes related to mantle dynamics may possibly have influenced some of the Palaeozoic orogenic belts, the lifespan of mountainous relief in these old orogenic belts remains a long-standing problem in Earth sciences³.

A concept that more accurately describes the physics of erosional processes in rivers involves a process-based formalism for bedrock incision by saltating sediment particles in a river^{5,24}. In this saltation–abrasion model, the erosion rate is a direct function of abrasion per particle impact multiplied by the frequency of impacts and a sediment-cover factor²⁴ (Methods). The model captures the complex role of sediment concentration for the bedrock erosion rate and is supported by recent catchment-scale observations²⁵ and longitudinal river profiles^{26,27}, but has yet to be tested against long-term landscape evolution at orogenic scales.

To explore the fundamental implications of feedbacks between hillslope erosion, sediment delivery and channel incision in a non-glacial setting, we performed computational experiments that couple the full physics of the saltation–abrasion model with a stochastic model for bedrock landsliding and multi-component sediment transport on hillslopes and in rivers (Methods). We apply the saltation–abrasion formalism to model fluvial incision because of its solid foundation in physical principles based on experiments^{5,24}, but our findings apply to all sediment-flux-dependent fluvial incision models. Bedrock landsliding is incorporated because threshold-dominated hillslope processes, such as landsliding, have a dominant role in limiting the relief in tectonically active regions^{9,11,20,21} and because landslide magnitude and frequency are critical for providing abrasive agents to the fluvial system^{10,11,16,17,28}. Landslides are important for regulating the erosion budget of tectonically active mountain ranges, which is most evident in the distinct threshold landscapes presently found, for example, in Taiwan²⁸ and the Himalayas^{20,21}. In addition to fluvial incision and bedrock landsliding, our computational experiments include slope-independent hillslope weathering, nonlinear hillslope sediment transport and grain-size-dependent sediment transport in rivers (Methods).

The computational experiments are designed to investigate primarily the coupled impact of bedrock landsliding controlled by threshold slopes and fluvial erosion driven by the sediment flux in rivers. We note that lithological contrasts not addressed by our model experiments also influence river incision rates, and that, depending on the geological setting, the rock hardness may increase when long-term erosion exposes the deep and resistant core of mountain belts. Furthermore, additional erosion processes in rivers and on hillslopes may be of relevance in natural systems. The feedbacks between landslides and river incision that we address here are likely to dominate in settings where sediment-bed impacts drive bedrock abrasion or accelerate quarrying by producing fractures in the bedrock, but their significance will be less important in settings where other processes, such as chemical weathering, dominate^{1,4}. The aim here, however, is to demonstrate the fundamental impact of feedbacks between landslides and saltation–abrasion on fluvial incision rates in the context provided by the necessity to reconcile rapid incision rates in tectonically active orogens with

¹Department of Geoscience, Aarhus University, Høegh-Guldbergs Gade 2, 8000 Aarhus C, Denmark. ²School of Earth Sciences, University of Melbourne, Victoria 3010, Australia.

the long-term survival of significant orogenic relief after cessation of tectonic activity. To do so, we model a cross-section through an asymmetric mountain range generated by tectonic rock uplift in the shape of a two-sided wedge system (Fig. 1). We focus on the influence of tectonic uplift on river erosion rates, and find that the results are independent of bedrock lithology as long as saltation–abrasion remains the dominant driver of river erosion. The spatially variable uplift rate allows us to study the influence of uplift rate on the resulting relief (Supplementary Fig. 2). To demonstrate the key feedbacks, we performed identical experiments using both the stream-power model and the saltation–abrasion model with the same coupling to bedrock landsliding and sediment transport in both models (Methods).

Our results confirm that fluvial incision by saltation–abrasion generates landscape morphologies very similar to those predicted by stream-power models and observed in fluvial systems²⁹. Channel profiles are upwards concave and drainage following the steepest topographic descent paths leads naturally to a system defined by catchments with large and gently dipping valleys and a number of steeper tributaries (Fig. 1). During the tectonically active phase, both the saltation–abrasion model and the stream-power model reach a topographic steady state in which tectonic rock uplift is balanced by erosion everywhere in the modelled landscape. Both models are associated with poorly constrained rate-limiting parameters (Methods), which we calibrate to obtain steady-state landscapes of similar mean ($\sim 1,100$ m) and maximum ($\sim 3,500$ m) elevations. The scale of this steady-state configuration resembles those of relatively small orogens like, for example, Taiwan or the Southern Alps. In the steady-state configuration, bedrock landsliding represents a primary erosion mechanism in both models because hillslopes are

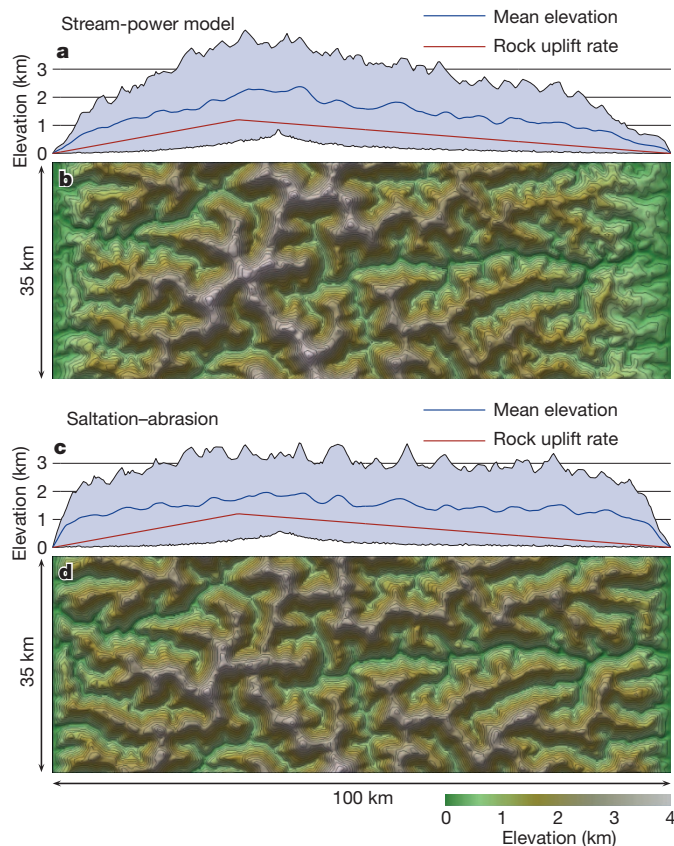


Figure 1 | Landscape morphology. **a**, Minimum, mean and maximum elevations along an east–west transect of the stream-power model. The red curve shows the variation in uplift rate, which peaks at 1 mm yr^{-1} . **b**, Detailed view of the resulting model landscape when bedrock landsliding is coupled to stream-power erosion. **c**, **d**, The same details, but for the saltation–abrasion model. The full model geometry is shown in Supplementary Fig. 4.

allowed to reach threshold slopes in many places (Supplementary Information and Supplementary Figs 2 and 3). The simulated landslide frequency-size distribution conforms to a power-law distribution (Supplementary Fig. 5), although the resolution of the numerical model limits the occurrence of small landslides. Of greater importance is, however, the bulk landslide erosion rate (Fig. 2), which represents the primary sediment flux from the hillslopes to the river network in the tectonically active phase.

Although the steady-state topographic patterns are largely similar for the two models, the temporal variations in erosion rate differ significantly. The saltation–abrasion model reveals a highly dynamic system with several feedbacks (Figs 2 and 3 and Supplementary Video 1). When the landslide frequency increases, rivers receive more sediment and accelerate fluvial incision while the landslide detritus is moved through the drainage network (Fig. 2). This further accelerates the landslide frequency because hillslopes steepen as the base level set by the channel elevation is lowered. This positive feedback terminates when excessive sediment supply protects the river bed from further erosion. At this point, fluvial incision slows, reducing the likelihood of landslides, and a negative feedback between fluvial erosion and landslides is established that helps to stabilize the relief temporarily (Fig. 2).

The pattern characterized by a highly oscillatory erosion flux during the active phase changes when tectonic activity ceases. At this point, continued rock uplift is due only to flexural-isostatic unloading, and the mean elevation of the landscape starts to decline. As hillslope gradients decrease below the critical threshold value for landsliding (Methods), the landslide frequency drops drastically (Fig. 3a). The landslide frequency decreases in our models simply because tectonic rock uplift no longer maintains the steep threshold slopes, and we note that the drop in landslide frequency may be even more dramatic in natural settings because earthquakes related to tectonic activity are

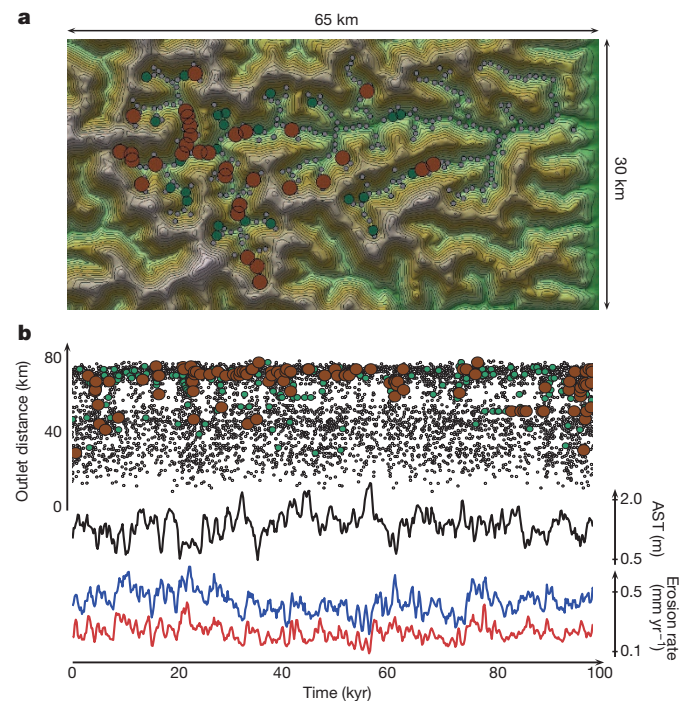


Figure 2 | Feedbacks between landsliding, fluvial incision and sediment transport. **a**, The location of large landslides in one of the model's major catchments during a 100-kyr period with tectonic uplift. The circles indicate the locations of the landslide initiation points. Circle size and colour indicate landslide volume (brown, $>0.3 \text{ km}^3$; green, $>0.2 \text{ km}^3$; grey, $>0.05 \text{ km}^3$). **b**, The temporal distribution of landslides (circles) with distance to catchment outlet along the vertical axis. The figure also shows catchment-averaged fluvial (red curve) and landslide (blue curve) erosion rates along with the averaged sediment thickness (AST) in the catchment (black curve).

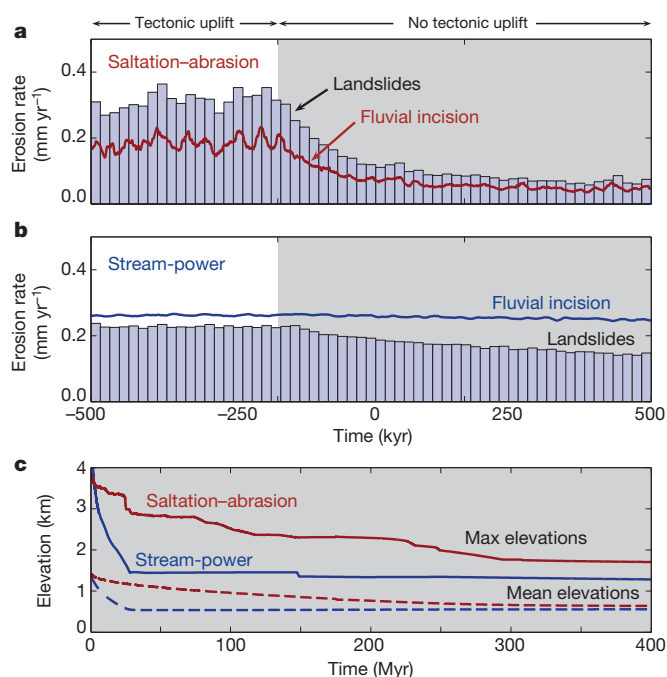


Figure 3 | Erosion rates and post-orogenic lifespan. **a**, Highly fluctuating erosion rates by saltation-abrasion and landsliding during the phase of tectonic uplift and slow erosion when tectonic activity stops. **b**, The combination of stream-power erosion and landslides does not include these feedbacks, and erosion rates are not directly affected by tectonic activity. The grey bars in **a** and **b** represent landslide erosion rates averaged over 10-kyr intervals. **c**, Results of model experiments covering 400 Myr of post-orogenic topographic evolution. The landscape of the saltation-abrasion model stays high for several hundred million years before a steady, transport-limited configuration is reached. The stream-power model achieves this configuration after only 25 Myr.

viewed as important landslide triggers¹¹. In the saltation-abrasion model, the decrease in landslide frequency leads to a corresponding decrease in the rate of fluvial incision, because of the associated decline in sediment input to the streams. The slowing fluvial erosion keeps channel elevations high and stalls both erosion processes by further reducing the landslide frequency. This is in stark contrast to the behaviour of the stream-power model (Fig. 3b), which exhibits a much more gradual decrease in erosion rate after tectonic uplift ceases, because the stream-power erosion rate is scaled only by the local channel slope and water discharge.

A sudden decrease in landslide frequency and saltation-abrasion erosion has a significant effect on the post-orogenic lifespan. Our scaled model results show that peaks can stand above an elevation of 2 km for more than 200 Myr following the cessation of tectonic activity (Fig. 3c). That contrasts with our scaled stream-power model in which elevations above 2 km last only 20 Myr because the stream-power erosion rates remain high in the absence of tectonic activity as long as significant relief persists. Both model experiments eventually terminate in similar transport-limited landscapes with main valleys that become permanently alluviated when the available stream power decreases below the threshold required for sediment transport³. At this stage, the two models converge, but the duration of the transition to a transport-limited stage differs by more than an order of magnitude because the mechanisms dictating the rate of post-orogenic river incision in the two models are fundamentally different. Landscapes in the stream-power model reach the transport-limited stage after only 25 Myr, whereas this transition takes more than ten times longer in the saltation-abrasion model. (Fig. 3c, Supplementary Information and Supplementary Fig. 4). These precise figures depend on the details of the parameterization, but the order-of-magnitude difference in post-orogenic topographical lifespan stands as a robust result of the different fluvial erosion mechanisms.

The prolonged lifespan of significant mountain-range topography in the saltation-abrasion model is caused by the reduced influx of sediment to the rivers³⁰ when tectonic activity stops, and we note that variations in the parameterization of saltation-abrasion, the sediment transport or the bedrock exposure estimates do not influence this result (Supplementary Fig. 6). Although other processes may substantially influence the post-orogenic lifespan in some geological settings, our results demonstrate that couplings between sediment-flux-dependent fluvial incision and threshold-dominated hillslope processes have the potential to explain the effects of tectonic uplift on long-term erosion rates^{1,2,17,19–21}. The interplay between hillslope processes and fluvial erosion by saltation-abrasion therefore provides a plausible physical mechanism for the preservation of several-hundred-million-year-old orogenic reliefs in tectonically inactive regions.

METHODS SUMMARY

The landscape evolution model used in this study computes the transport of water and sediment across a plan-form grid consisting of irregularly distributed Voronoi cells. Connecting neighbouring cells in the direction of steepest descent generates the fluvial surface transport network. Topographical depressions, which may for example arise from dams generated by landslides, are filled by water that form lakes and ensure continuous drainage from every grid cell to the model boundaries.

The rate of fluvial incision into bedrock is calculated from either the saltation-abrasion model or the stream-power model. For computing saltation-abrasion, we include the full physics of the model²⁴. Both types of fluvial erosion model are coupled to models for bedrock landsliding, sediment transport in rivers and on hillslopes, long-term hillslope weathering, and flexural isostasy. The various erosion components are coupled through their effects on bedrock topography and their contributions to a layer of transportable sediment. The fluvial sediment transport model operates with sediment of varying grain sizes to incorporate the effects of downstream fining on sediment transport capacity and saltation-abrasion erosion rate. The hillslope sediment transport model is independent of grain size, but includes nonlinear effects of slope. See Methods and Supplementary Information for additional references and more details on all model components.

Full Methods and any associated references are available in the online version of the paper.

Received 23 January; accepted 22 April 2013.

- Von Blanckenburg, F. The control mechanisms of erosion and weathering at basin scale from cosmogenic nuclides in river sediment. *Earth Planet. Sci. Lett.* **237**, 462–479 (2005).
- Molnar, P., Andersen, R. S. & Anderson, S. P. Tectonics, fracturing of rock, and erosion. *J. Geophys. Res.* **112**, F03014 (2007).
- Baldwin, J. A., Whipple, K. X. & Tucker, G. E. Implications of the shear stress river incision model for the timescale of postorogenic decay of topography. *J. Geophys. Res.* **108**, 2158 (2003).
- Whipple, K. X., Hancock, G. S. & Anderson, R. S. River incision into bedrock: mechanics and relative efficacy of plucking, abrasion, and cavitation. *Geol. Soc. Am. Bull.* **112**, 490–503 (2000).
- Sklar, L. S. & Dietrich, W. E. Sediment and rock strength controls on river incision into bedrock. *Geology* **29**, 1087–1090 (2001).
- Hancock, G. S. & Anderson, R. S. Numerical modelling of fluvial strath-terrace formation in response to oscillating climate. *Geol. Soc. Am. Bull.* **114**, 1131–1142 (2002).
- Turowski, J. M., Lague, D. & Hovius, N. Cover effects in bedrock abrasion: a new derivation and its implications for the modelling of bedrock channel morphology. *J. Geophys. Res.* **112**, F04006 (2007).
- Yanites, B. J. *et al.* The influence of sediment cover variability on long-term river incision rates: an example from Peikang River, central Taiwan. *J. Geophys. Res.* **116**, F03016 (2011).
- Larsen, I. J. & Montgomery, D. R. Landslide erosion coupled to tectonics and river incision. *Nat. Geosci.* **5**, 468–473 (2012).
- Quimet, W. B. *et al.* The influence of large landslides on river incision in a transient landscape: eastern margin of the Tibetan Plateau (Sichuan, China). *Geol. Soc. Am. Bull.* **119**, 1462–1476 (2007).
- Korup, O., Densmore, A. L. & Schlunegger, F. The role of landslides in mountain range evolution. *Geomorphology* **120**, 77–90 (2010).
- Seidl, M. A. & Dietrich, W. E. The problem of channel erosion into bedrock. *Catena* (Suppl.) **23**, 101–124 (1992).
- Howard, A. D. & Kerby, G. Channel changes in badlands. *Geol. Soc. Am. Bull.* **94**, 739–752 (1983).
- Whipple, K. X. *et al.* Geomorphic limits to climate-induced increases in topographic relief. *Nature* **401**, 39–43 (1999).
- Kirby, E. & Whipple, K. X. Quantifying differential rock-uplift rates via stream profile analysis. *Geology* **29**, 415–418 (2001).

16. Dadson, S. J. *et al.* Links between erosion, runoff variability and seismicity in the Taiwan orogen. *Nature* **426**, 648–651 (2003).
17. Stock, J. D. *et al.* Field measurements of incision rates following bedrock exposure: implications for process controls on the long profiles of valleys cut by rivers and debris flow. *Geol. Soc. Am. Bull.* **117**, 174–194 (2005).
18. Riebe, C. S. *et al.* Minimal climatic control on erosion rates in the Sierra Nevada. *Calif. Geol.* **29**, 447–450 (2001).
19. Burbank, D. W. *et al.* Decoupling of erosion and precipitation in the Himalayas. *Nature* **426**, 652–655 (2003).
20. Burbank, D. W. *et al.* Bedrock incision, rock uplift and threshold hillslopes in the northwestern Himalayas. *Nature* **379**, 505–510 (1996).
21. Montgomery, D. R. & Brandon, M. T. Topographic controls on erosion rates in tectonically active mountain ranges. *Earth Planet. Sci. Lett.* **201**, 481–489 (2002).
22. von Blanckenburg, F., Hewawasam, T. & Kubik, P. W. Cosmogenic nuclide evidence for low weathering and denudation in the wet, tropical highlands of Sri Lanka. *J. Geophys. Res.* **109**, F03008 (2004).
23. Scharf, T. E. *et al.* Strong rocks sustain ancient postorogenic topography in southern Africa. *Geology* **41**, 331–334 (2013).
24. Sklar, L. S. & Dietrich, W. E. A mechanistic model for river incision into bedrock by saltating bed load. *Wat. Resour. Res.* **40**, W06301 (2004).
25. Cowie, P. A. *et al.* New constraints on sediment-flux-dependent river incision: implications for extracting tectonic signals from river profiles. *Geology* **36**, 535–538 (2008).
26. Whipple, K. X. & Tucker, G. E. Implications of sediment-flux-dependent river incision models for landscape evolution. *J. Geophys. Res.* **107**, 2039 (2002).
27. Gasparini, N. M., Whipple, K. X. & Bras, R. L. Predictions of steady state and transient landscape morphology using sediment-flux-dependent river incision models. *J. Geophys. Res.* **112**, F03S09 (2007).
28. Hovius, N., Stark, C. P., Hao-Tsu, C. & Jiun-Chuan, L. Supply and removal of sediment in a landslide-dominated mountain belt: Central Range, Taiwan. *J. Geol.* **108**, 73–89 (2000).
29. Sklar, L. S. & Dietrich, W. E. Implications of the saltation-abrasion bedrock incision model for steady-state river longitudinal profile relief and concavity. *Earth Surf. Process. Landf.* **33**, 1129–1151 (2008).
30. Jansen, J. D. *et al.* Does decreasing paraglacial sediment supply slow knickpoint retreat? *Geology* **39**, 543–546 (2011).

Supplementary Information is available in the online version of the paper.

Acknowledgements D.L.E. acknowledges funding from the Danish Council for Independent Research under the Sapere Aude programme. M.F.K. acknowledges funding from the Carlsberg Foundation and the Villum Foundation. M.S. acknowledges funding from ARC DP110104098 and AISRF.

Author Contributions D.L.E. developed the computational modelling scheme and performed the modelling. All authors contributed equally to the design of the study and the writing of the paper.

Author Information Reprints and permissions information is available at www.nature.com/reprints. The authors declare no competing financial interests. Readers are welcome to comment on the online version of the paper. Correspondence and requests for materials should be addressed to D.L.E. (david@geo.au.dk).

METHODS

River dynamics. We modelled fluvial erosion and sediment transport across a two-dimensional plan form grid consisting of irregularly distributed Voronoi cells. The river pathways were established by connecting neighbouring cells in the direction of steepest descent in every time step following the CASCADE algorithm³¹. The precipitation rate, p_r , was uniform across the grid, implying that the volumetric water flux was $Q_w = p_r A$, where A is the upstream catchment area.

We followed ref. 32 in calculating the average bed shear stress as $\tau_b = \rho_w (g Q_w S)^{2/3} W^{-2/3}$, where ρ_w is the density of water, g is the acceleration due to gravity and S is the channel slope. The channel width, $W = k_w Q_w^{1/2}$, is a function of surface water discharge where k_w is a constant channel-width scaling factor³² (see Supplementary Table 1 for values of all model parameters).

Sediment transport. The applied landscape evolution model transports sediments in rivers and on hillslopes. The computational experiments therefore included a layer of mobile sediment of thickness H_s . The thickness of this sediment layer was updated by solving the continuity equation for volume conservation

$$\frac{\partial H_s}{\partial t} = -\nabla \cdot (q_{sf} + q_{sh}) + \frac{\rho_r}{\rho_s} (\dot{E}_f + \dot{E}_l + \dot{E}_h)$$

where q_{sf} and q_{sh} are the sediment flux vectors in rivers and on hillslopes, respectively; ∇ is the gradient operator; ρ_r and ρ_s are the densities of bedrock and sediment, respectively; and \dot{E}_f , \dot{E}_l and \dot{E}_h are the bedrock erosion rates due to rivers, landslides and hillslope weathering, respectively. These erosion mechanisms are described in separate sections below.

For the downstream sediment flux in rivers (q_{sf}), the transport model operated with sediment of varying grain sizes. This made it possible to incorporate the effects of downstream fining on sediment transport and bedrock erosion by saltation–abrasion. The total sediment volume was therefore binned according to grain size (D) from $\psi = 0, 1, 2, \dots, 8$, where $\psi = \log_2(D/D_0)$ is a logarithmic grain-size distribution³³ (Supplementary Table 2) and $D_0 = 1$ mm is a reference grain size. The sediments were then transported by the two-fraction model of ref. 34, in which the different grain sizes are combined in two groups: mixed sand ($D \leq 2$ mm) and mixed gravel ($D \geq 2$ mm). Carrying capacities for sand and gravel were calculated from the two-fraction model and rivers were assumed to run at capacity if enough sediment was available (see Supplementary Information for more information on the fluvial sediment transport model).

For sediment transport on hillslopes, we used a nonlinear flux model^{35,36} relating volumetric sediment flux, q_{sh} , to the bed gradient, ∇b :

$$q_{sh} = -K_s \frac{\nabla b}{1 - (|\nabla b|/s_c)^2}$$

where s_c is the critical slope and K_s is a constant (Supplementary Table 1). In this model, sediment transport is inefficient on flat surfaces and more efficient on steep slopes that approach the critical value, s_c .

River erosion by saltation–abrasion. The saltation–abrasion erosion rate, \dot{E}_f^{sa} , is expressed as the product of three terms²⁴, $\dot{E}_f^{sa} = V_i I_r F_c$, where V_i is the average volume of bedrock detached per particle impact; I_r is the rate of particle impact per unit area and F_c (the sediment cover factor) is the fraction of the river bed that is free of sediment and therefore exposed to erosion.

We followed the approach of ref. 24 closely, and consequently approximated \dot{E}_f^{sa} with

$$\dot{E}_f^{sa} = K_{sa} \frac{q_{sf}^{\psi}}{W} F_c (\tau' / \tau_c' - 1)^{-0.52} |1 - (u' / w_f)|^{1.5}$$

where K_{sa} is a lumped scaling parameter (Supplementary Information and Supplementary Table 1), q_{sf}^{ψ} is the sediment flux of a particular grain size, τ' is the non-dimensional Shield's stress, τ_c' is the non-dimensional critical threshold shear stress for sediment entrainment, $u' = \sqrt{\tau_b / \rho_w}$ is the shear velocity and w_f is the settling velocity of sediment grains. The sediment-free fraction of the river bed, F_c , was assumed to vary linearly between two endmember cases: (1) when the river runs at capacity and the bed is fully alluviated ($V_t = \Delta t Q_t$, where V_t is the volume of sediment available for transport, Q_t is the sediment transport capacity of the river segment and Δt is the length of the time step), and (2) when the river receives no sediment that can form patches of alluvial cover ($V_t = 0$):

$$F_c = \begin{cases} 1 - V_t / \Delta t Q_t & \text{for } V_t < \Delta t Q_t \\ 0 & \text{otherwise} \end{cases}$$

Importantly, apart from the sediment carried by the river, V_t includes sediment deposited on the river bed, which ensures that sediment not in transport also influences the sediment cover factor. Additional experiments with other types of functional form for F_c show that our conclusions are robust with respect to such variations (Supplementary Fig. 6).

The saltation–abrasion rate, \dot{E}_f^{sa} , depends on grain size, and we therefore computed the total erosion rate by summing the contributions to the erosion rate associated with the individual sediment grain-size bins (Supplementary Table 2). The values of q_{sf}^{ψ} , τ' , τ_c' and w_f were therefore calculated separately for each sediment grain size (see Supplementary Information for details on the grain-size dependence and for the full derivation of the saltation–abrasion relations above).

Stream-power erosion. For the model experiments using stream-power erosion, the fluvial erosion rate was calculated from $\dot{E}_f^{sp} = K_{sp} F_c Q_w^m S^n$, where K_{sp} is a rate-limiting constant³⁷, Q_w is the water discharge (volumetric flux), S is the channel slope, and m and n are constants (Supplementary Table 2). We note that we included in the stream-power model the protecting effect of sediment cover by incorporating F_c from the saltation–abrasion theory. By including the same protecting effects of sediments in all experiments, we effectively isolated the differences between the two incision models (saltation–abrasion and stream-power erosion). For example, by incorporating F_c in both models, we made sure that transport thresholds affected both model types similarly.

Bedrock landslides. We used the model in ref. 38 for simulating bedrock landslides. The model is stochastic in the sense that the probability of hillslope failure depends on the Culmann slope stability criterion³⁸. The Culmann criterion predicts the maximum stable height of a hillslope, H_c , from the angle of internal friction, ϕ , the hillslope cohesion, C , and the hillslope angle, β :

$$H_c = \frac{4C \sin(\beta) \cos(\phi)}{\rho_s g (1 - \cos(\beta - \phi))}$$

In every time step of the model run, a fixed number, N_c , of random cells were checked for landsliding. From each of these cells (target cells), the maximum extent of a stable plane was mapped by recursively collecting in a list the upslope cells with elevations above the cone-shaped plane that dips with angle ϕ and passes through the target cell. The stable plane must be continuous, meaning that only cells that neighbour a cell already on the list was added to the list.

After the list was generated, the hillslope height, H , and the hillslope angle, β , were established from the maximum elevation difference between the target cell and cells on the list. The failure probability was computed as $p_{fail} = H/H_c$. The hillslope fails if a randomly generated number between 0 and 1 falls below p_{fail} .

If failure occurred, the angle of the failure plane³⁸ was calculated from $\theta = (\beta + \phi)/2$. The failure plane was mapped by repeating the recursive procedure, now listing the cells with elevations above the cone-shaped failure plane dipping at angle θ . The rock mass above the failure plane was eroded and passed to the target cell as new sediment.

We assumed that the sediment generated in a landslide has a fractal distribution of grain sizes³⁹, such that $N_{\psi} \propto D_{\psi}^{-f}$, where N_{ψ} is the number of particles with diameter greater than D_{ψ} (Supplementary Table 2) and $f = 2.65$ is the fractal dimension⁴⁰. The fractal distribution was used to constrain the volume distribution of grain sizes within a landslide deposit: $V_s(\psi) = w_{\psi} V_{\text{landslide}}$, where $V_{\text{landslide}}$ is the total sediment volume generated by the landslide and w_{ψ} is the volume weight function associated with each grain-size bin ψ (Supplementary Table 2). We note that the volume weights were calculated to satisfy the fractal distribution.

Hillslope weathering. We followed ref. 38 by including nonlinear sediment (regolith) production to simulate slow hillslope erosion on bare bedrock surfaces⁴¹ (where $H_s = 0$), faster erosion under moderate sediment thicknesses⁴² ($H_s \leq H_s'$) and decreasing erosion rates under larger sediment thicknesses⁴³ ($H_s > H_s'$). In this model, the bedrock erosion rate is

$$\dot{E}_h = \begin{cases} \dot{E}_c + \frac{\dot{E}' - \dot{E}_0}{H_s'} H_s & \text{for } 0 \leq H_s < H_s' \\ \dot{E}' \exp\left(\frac{H_s' - H_s}{\Delta H}\right) & \text{for } H_s \geq H_s' \end{cases}$$

All parameters are listed in Supplementary Table 1.

We assumed that the grain sizes of the sediments produced by weathering is of the same fractal distribution as for landsliding, and the volume weights of Supplementary Table 2 were therefore reused. We note that grain sizes are likely to be smaller for sediments generated by weathering than by landsliding. However, using the same grain sizes for both erosion processes is a conservative assumption, because the saltation–abrasion erosion process preferentially weights the coarser fractions. Reducing sediment grain sizes for weathering would therefore further lower saltation–abrasion rates and amplify the difference between the saltation–abrasion and stream-power models.

Flexural isostasy. Flexural isostatic adjustments, $W_i(x, y)$, in response to erosional unloading and sediment deposition were performed according to the two-dimensional elastic thin-plate equation:

$$\frac{\partial^4 W_i}{\partial x^4} + 2 \frac{\partial^4 W_i}{\partial x^2 \partial y^2} + \frac{\partial^4 W_i}{\partial y^4} = \frac{L(x, y)}{D_i}$$

Here $D_f = YT_c^3/12(1 - \nu^2)$ is the flexural rigidity, Y is Young's modulus, ν is the Poisson ratio and T_c is the elastic thickness of the lithosphere (Supplementary Table 1). $L(x, y) = \rho_s g E(x, y) - \rho_s g H_s(x, y) - \rho_a g W_f(x, y)$ is the vertical load on the plate (positive upward), where $E(x, y)$ is the total bedrock erosion in each model cell, H_s is the amount of sediment present and ρ_a is the density of the isostatically compensating asthenosphere rocks.

31. Braun, J. & Sambridge, M. Modelling landscape evolution on geological time scales: a new method based on irregular spatial discretization. *Basin Res.* **9**, 27–52 (1997).
32. Tucker, G. E. & Slingerland, R. L. Predicting sediment flux from fold and thrust belts. *Basin Res.* **8**, 329–349 (1996).
33. Parker, G. & Andrews, E. D. Sorting of bedload sediment by flow in meander bends. *Wat. Resour. Res.* **21**, 1361–1373 (1985).
34. Wilcock, P. R. Two-fraction model of initial sediment motion in gravel-bed rivers. *Science* **280**, 410–412 (1998).
35. Andrews, D. J. & Bucknam, R. C. Fitting degradation of shoreline scarps by a nonlinear diffusion model. *J. Geophys. Res.* **92**, 12857–12867 (1987).
36. Roering, J. J., Kirchner, J. W. & Dietrich, W. E. Evidence for nonlinear, diffusive sediment transport and implications for landscape morphology. *Wat. Resour. Res.* **35**, 853–870 (1999).
37. Howard, A. D. A detachment-limited model of drainage basin evolution. *Wat. Resour. Res.* **30**, 2261–2285 (1994).
38. Densmore, A. L., Ellis, M. A. & Anderson, R. S. Landsliding and the evolution of normal-fault-bounded mountains. *J. Geophys. Res.* **103**, 15203–15219 (1998).
39. Turcotte, D. *Fractals and Chaos in Geology and Geophysics* 20–34 (Cambridge Univ. Press, 1992).
40. Crosta, G., Frattini, P. & Fusi, N. Fragmentation in the Val Pola rock avalanche, Italian Alps. *J. Geophys. Res.* **112**, F01006 (2007).
41. Small, E. E., Anderson, R. S. & Hancock, G. S. Estimates of the rate of regolith production using ^{10}Be and ^{26}Al from an alpine hillslope. *Geomorphology* **27**, 131–150 (1999).
42. Ahnert, F. Brief description of a comprehensive three-dimensional process-response model of landform development. *Z. Geomorphol.* **24**, 11–22 (1970).
43. Heimsath, A. M., Dietrich, W. E., Nishiizumi, K. & Finkel, R. C. The soil production function and landscape equilibrium. *Nature* **388**, 358–361 (1997).